Quasi-monocrystalline silicon for low-noise end mirrors in cryogenic gravitational-wave detectors

Frank M. Kiessling,¹ Peter G. Murray,² Maya Kinley-Hanlon,² Iryna Buchovska,¹ Torunn K. Ervik,^{1,3} Victoria Graham,² Jim Hough,² Ross Johnston,² Mike Pietsch,¹ Sheila Rowan,² Roman Schnabel,⁴ Simon C. Tait,² Jessica Steinlechner,^{2,4,5,6} and Iain W. Martin²

¹Leibniz-Institut für Kristallzüchtung, Max-Born-Str. 2, D-12489 Berlin, Germany

²SUPA, School of Physics and Astronomy, University of Glasgow, Glasgow, G12 8QQ, Scotland

³National Institute of Occupational Health, Gydas vei 8, N-0363 Oslo, Norway

⁴Institut für Laserphysik und Zentrum für Optische Quantentechnologien,

Universität Hamburg, Luruper Chaussee 149, D-22761 Hamburg, Germany

⁵Maastricht University, P.O. Box 616, 6200 MD Maastricht, The Netherlands

⁶Nikhef, Science Park 105, 1098 XG Amsterdam, The Netherlands

(Dated: May 12, 2022)

Mirrors made of silicon have been proposed for use in future cryogenic gravitational-wave detectors, which will be significantly more sensitive than current room-temperature detectors. These mirrors are planned to have diameters of $\approx 50\,\mathrm{cm}$ and a mass of $\approx 200\,\mathrm{kg}$. While single-crystalline float zone silicon meets the requirements of low optical absorption and low mechanical loss, the production of this type of material is restricted to sizes much smaller than required. While conventional Czochralski silicon does not meet the required low absorption, magnetic field applied Czochralski silicon is a promising option, however may not be able to be produced with the required diameter. Here we present studies of silicon produced by directional solidification. This material can be grown as quasi-monocrystalline ingots in sizes larger than currently required. We present measurements of a low room-temperature and cryogenic mechanical loss comparable to float zone silicon. While the optical absorption of our test sample was significantly higher than required, the low mechanical loss motivates research into further absorption reduction in the future.

PACS numbers: 04.80.Nn, 42.79.Bh, 42.79.Wc, 78.66.Jg

I. INTRODUCTION

Since 2015, Advanced LIGO [I] and Advanced ⁵⁷ Virgo [2] have detected many gravitational-wave signals. ⁵⁸ During the first two observing runs, ten binary black hole ⁵⁹ mergers and one binary neutron star merger were ob- ⁶⁰ served [3]. KAGRA, a third generation detector, went ⁶¹ online during the third observing run [4], by the end of ⁶² which, 90 additional gravitational-wave detections were ⁶³ reported [5], [6], including signals originating from binary ⁶⁴ neutron stars, binary black holes and possibly neutron- ⁶⁵ star/black-hole binaries.

Gravitational-wave detectors are km-scale interferom- ⁶⁷ eters which measure relative strains in space induced by ⁶⁸ passing gravitational waves. Highly-reflective coated mir- ⁶⁹ rors form the core components of these instruments, with ⁷⁰ the detector monitoring the relative separation of the ⁷¹ mirrors in two perpendicular arms. Advanced LIGO and ⁷² Advanced Virgo, detectors of the second generation, op- ⁷³ erate at room temperature using mirror substrates made ⁷⁴ of fused silica (SiO₂). KAGRA is the first detector op- ⁷⁵ erating at cryogenic temperatures, designed to further ⁷⁶ reduce the thermal noise of the mirrors and their highly- ⁷⁷ reflective coatings [7].

The mechanical loss, which determines the magnitude 79 of the thermal noise, of fused silica increases by several or- 80 ders of magnitude when cooling from room temperature 81 to $\approx 20\,\mathrm{K}$ §. A different material is therefore required 82 for the mirror substrates in a cryogenic detector. While $_{83}$

KAGRA uses sapphire [9], other planned detectors such as LIGO Voyager [10] and the Einstein Telescope [11] are likely to use crystalline silicon.

To avoid heating from the laser light used for displacement sensing and to maintain cryogenic temperature, a mirror material with low optical absorption is essential. Single-crystalline silicon with a low level of doping and impurities (i.e. high resistivity) can have a low optical absorption at wavelengths $\gtrsim 1400\,\mathrm{nm}$ [12] [13]. The purity level required for gravitational-wave detectors can be provided by silicon produced with the float zone method. This type of silicon has also been shown to have low mechanical loss, resulting in low thermal noise, particularly at low temperatures [14]. However, the production of float zone silicon with diameter of $\approx 20\,\mathrm{cm}$ is already very technically challenging and therefore the realization of larger-diameters is unlikely [15].

From a thermal-noise perspective, Czochralski-grown (Cz) silicon, which can be grown in diameters of up to 45 cm [16], would also be a suitable material, but this type of silicon shows a higher level of impurities [17], resulting in a high absorption [13] which is incompatible with gravitational-wave detector mirrors. Magnetic field applied Czochralski (MCz) silicon, which has a reduced oxygen content in particular [18], has been observed to show low absorption and may be a promising way forward for gravitational-wave detection, if large enough diameters of substrate can be produced [19].

Another way to produce silicon ingots in the required

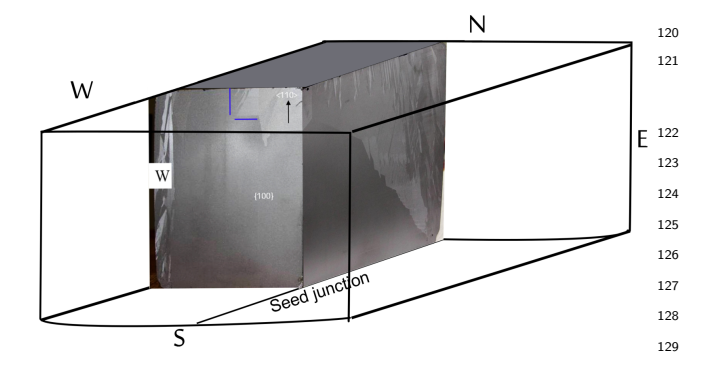


FIG. 1. Picture of the sandblasted G2 1/4 ingot sized $195 \times_{131}$ $195 \times 220 \,\mathrm{mm}^3$. The drawing illustrates the position of the block in relation to the 2 seed plates (bottom plane). W-N- $_{133}$ E-S are typically used marker to identify the position of the ingot to possible thermal asymmetries of the furnace, which $_{135}^{136}$ might influence the growth process.

84

85

87

90

91

92

93

95

96

97

99

101

102

104

105

106

107

108

109

110

111

112

113

115

116

118

137

138

large sizes may be growth by directional solidification,140 which results in a quasi-monocrystalline material. In¹⁴¹ this process, single crystalline seed plates cut from a Cz-142 grown silicon boule cover the bottom of a $\rm Si_3N_4$ coated 143 quartz crucible, and polycrystalline silicon fragments are144 filled in on top of these plates. The standard industrial 145 silicon feedstock charge of G6 ingots is about 800 kg with $^{\scriptscriptstyle 146}$ an ingot heights of 35 cm. G stands for 'generation' of 147 directional solidification technology and the number con-148 tains information about the squared ingot size, e.g. num-149 ber 6 means that the ingot can be cut into 6×6 bricks¹⁵⁰ for wafer slicing of standard solar cells with 156 mm \times^{151} 156 mm in size. This G-terminology is also used for fur-152 naces and crucibles. Except for the seeds, the silicon is 153 completely melted and then directionally solidified from 154 the bottom of the melt upward. The process attempts to 155 transfer the single-crystalline structure of the Cz seeds¹⁵⁶ to the ingot. Dislocation formation and multiplication is 157 still an unsolved problem in the crystallization of quasi¹⁵⁸ mono ingots.

In this article we present mechanical loss and opti-161 cal absorption measurements of samples cut from a G2162 quasi-monocrystalline silicon ingot. The mechanical loss¹⁶³ of our test samples was found to be comparable to that 164 of high-purity float zone silicon, which is usually in the 165 range of $10^{-8} - 10^{-9}$. However, the optical absorption at ¹⁶⁶ 1550 nm was found to be at a high level of several per-167 cent per centimeter, while the requirement is thought to 168 be $\lesssim 5 - 10 \times 10^{-6}$ /cm. The high absorption was not 169 unexpected as the material was doped and not optimized 170 for low optical absorption. Further work on absorption₁₇₁ reduction is of high interest. However, even with high₁₇₂ absorption, quasi-monocrystalline silicon may be a can-173 didate material for the 'end test mass' (ETM) mirrors₁₇₄ in gravitational-wave detectors, through which only very 175 low laser power is transmitted.

II. QUASI-MONO GROWTH TECHNIQUE AND SAMPLE PREPARATION

The quasi-monocrystalline silicon investigated here was originally grown for solar-cell production. The material was grown using two (110)-orientated single crystalline seeds from Cz crystals, which were closely placed at the bottom of the G2-sized quartz crucible. The inner crucible walls were Si₃N₄ coated to prevent sticking with the silicon ingot. To obtain p-type material with a target resistivity of $0.9 \Omega cm$ for solar cells, highly boron doped silicon wafer pieces with a specific resistivity of $0.0145\,\Omega\mathrm{cm}$ together with silicon feedstock were placed on top of the seeds. The melting process of the feedstock was carefully controlled until an equilibrium of the melt and the partially molten seeds was established. The solidification was initiated from bottom to top by a rapid temperature decrease. The growth process was carried out in a G2-sized directional solidification furnace equipped with KRISTMAG® heater-magnet modules, which are able to produce heat and magnetic fields at the same time. A downward travelling 10 Hz oscillating magnetic field was applied to ensure a sufficient mixing of the melt by flow control. The average solidification velocity was determined to be $0.8 - 0.9 \,\mathrm{cm/h}$. More details about the use of the travelling magnetic field and growth velocity determination in this furnace were described by Linke et al. 20. A quasi-monocrystalline ingot was obtained and then guartered. It is clearly seen from the depicted northwest quarter in Fig. 1 that this ingot is only partially single crystalline.

The crystal orientation of the seeds was mostly transferred to the growing ingot at the beginning of the solidification process. The single crystalline growth was strongly influenced by secondary grain growth from the crucible walls and formation of grains at twin boundaries (twins) [21] visible by different shades of grey.

The selection of the samples investigated here was based on two main criteria. First, the material had to be monocrystalline and second, the oxygen and carbon concentrations had to be as low as possible. Due to their different segregation behaviour, the oxygen concentration decreases along the growth direction from the bottom to the top of the ingot while the carbon concentration increases [22, 23]. These concentrations were measured in the overall characterisation of the grown ingot on an adjacent longitudinal cut along the growth direction using FTIR spectroscopy (see Sec. \boxed{V}). In the sample selection area, the substitutional carbon concentration $[C_s] = 1 - 3 \times 10^{17} \, \mathrm{cm}^{-3}$ and the interstitial oxygen concentration $[O_i] = 3 - 2 \times 10^{17} \, \mathrm{cm}^{-3}$ were measured at a scan distance of 1 cm.

Two single crystalline samples of $40 \times 15 \times 15 \text{mm}^3$ (named 'small QM cuboid') and $80 \times 80 \times 15 \text{ mm}^3$ were cut from the central part as indicated in Fig. [2]. From the bigger cuboid, a 50.8 mm diameter \times 5 mm thick disk was cut (named 'QM disk'). Both samples were polished to be used for optical absorption and mechanical loss mea-

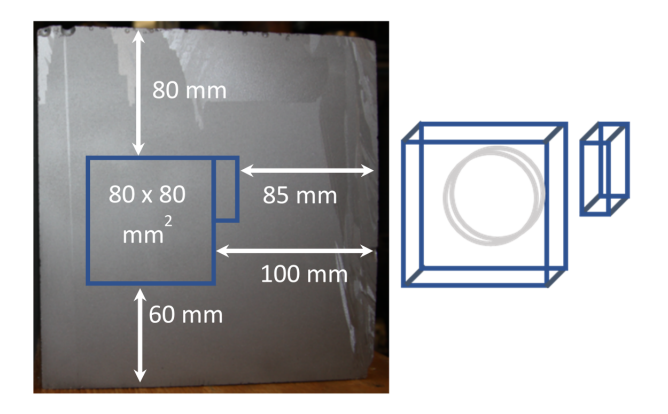


FIG. 2. left: Sample position marked on the {100} vertical cut of a G2 $\frac{1}{4}$ ingot and right: Drawing of the final $\varnothing \, 50.8 \times 5 \, \mathrm{mm}$ thick disk (gray - QM disk) inside the bigger single crystalline cuboid, and the position of the smaller sample (small QM cuboid) for absorption measurements.

177 surements, respectively.

178

179

180

181

182

183

184

185

186

187

188

189

190

191

192

193

195

196

197

198

199

201

202

204

205

207

208

210

III. MECHANICAL LOSS MEASUREMENTS

Mechanical loss is a measure of the magnitude of internal friction in a material. The thermal displacement noise arising from a mirror substrate in a gravitational wave detector (in $m/\sqrt{\rm Hz}$) is proportional to the square₂₁₂ root of the mechanical loss of the mirror material. The mechanical loss of a number of resonant modes of the $\langle 100 \rangle$ -oriented QM disk was measured using a Gentle Nodal Suspension (GeNS) system [24], and compared to the mechanical loss of a float zone $\langle 111 \rangle$ silicon sample of²¹³ the same dimensions (named 'FZ disk'). Previous work²¹⁴ by Nawrodt et al. on similar geometries of silicon sub-²¹⁵ strates showed almost identical loss between 30 K and²¹⁶ 200 K for these different crystal orientations [25].

Figure 3 shows a photo of the setup used for cryogenic²¹⁸ mechanical loss measurements. The disk (top of the pic-219 ture) being measured was balanced on a silicon spherical lens with a radius of curvature of 60.44 mm, where it balanced freely throughout the measurements. The cryostat²²⁰ chamber was evacuated to pressures below 10^{-5} mbar, and the mechanical resonances of the samples were ex-221 cited via comb-shaped capacitor exciter plates, visible²²² underneath the bottom-left of the substrate in Fig. 3,223 placed $\sim 1 \, \mathrm{mm}$ away from the surface of the disks. The₂₂₄ resonant modes of the disks are excited by applying a225 high-voltage a.c. signal to the exciter plate, sweeping²²⁶ slowly over the frequency of the mode. After a mode is₂₂₇ excited the excitation voltage is turned off, and the vi-228 bration of the sample is left to decay. The motion of the229 sample is measured by reflecting a laser beam from the 230 face of the sample onto a split-photodiode sensor, which₂₃₁ provides a signal proportional to the amplitude of the232 motion. The loss, $\phi(\omega_0)$, of the resonant mode of angu-233 lar frequency ω_0 , is calculated from the exponential decay₂₃₄

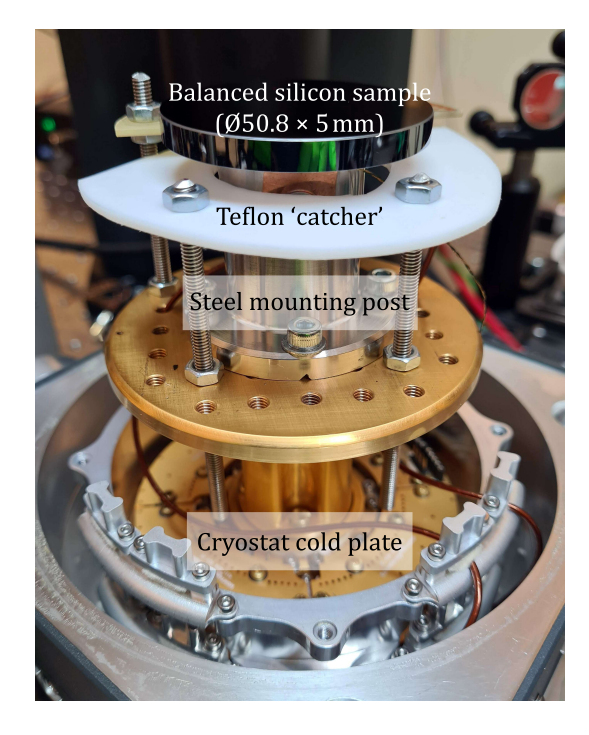


FIG. 3. Image of the $\langle 100 \rangle$ -oriented QM disk balanced on top of a rounded silicon lens inside the $10 \times 10 \, \mathrm{cm}^2$ experimental chamber of the Montana Instruments s100 Cryostation.

of the excited amplitude, which follows the form

$$A(t) = A_0 e^{(-\phi(\omega_0)\omega_0 t/2)} \tag{1}$$

where A(t) is the amplitude at a time t and A_0 is the initial amplitude after the excitation is turned off.

Figure 4 shows the resonant mode shapes of six resonant modes (14.7, 17.8, 36.0, 36.0, 60.1 and 87.8 kHz) at room temperature of the QM disk. For the FZ disk, the mode frequencies differ due to the difference in crystal orientation.

A. Mechanical loss at room temperature

Initially, the mechanical loss of the QM and FZ disks was measured at room temperature. The loss of each resonant mode was measured multiple times, with the average loss calculated and the error taken as the standard deviation. Each disk was re-balanced on the nodal support several times and the loss measurements repeated. For each resonant mode we present the lowest loss obtained from the repeated suspensions, as is standard in loss measurements. The results are shown in Fig. [5] (see values at 290 K for room temperature measurements).

For both disks, all measured losses are below 1×10^{-6} . For the modes at $14.75\,\mathrm{kHz}$ and $17.85\,\mathrm{kHz}$, the room-temperature loss of the QM disk is lower than that of the two lowest resonant frequencies of the FZ disk, while

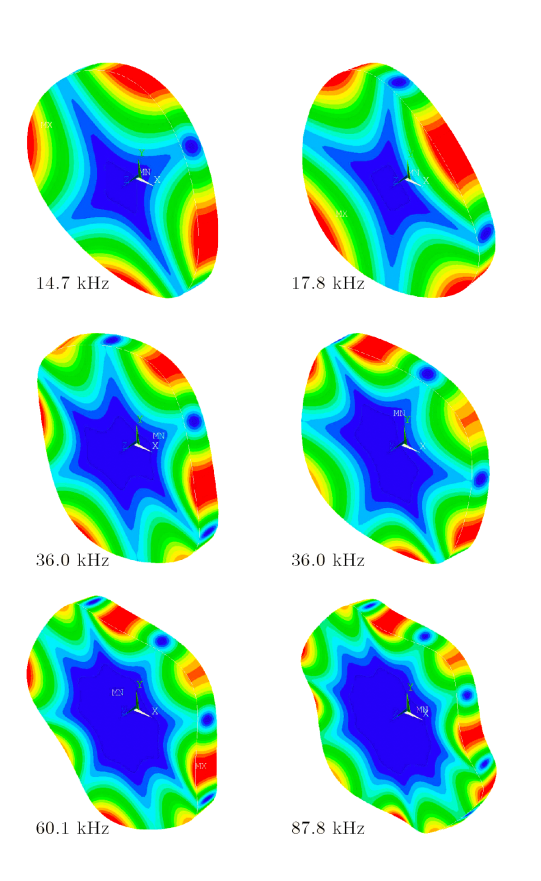


FIG. 4. Total surface deformation of the resonance modes of the $\langle 100 \rangle$ -orientated QM disk, calculated using finite element analysis. The blue corresponds to regions of least motion and the red to regions of greatest motion.

for the modes around $36\,\mathrm{kHz}$, the loss of the FZ disk is₂₈₆ lower. For the QM disk, also a mode at about $60\,\mathrm{kHz}$ was₂₈₇ measured which shows a loss similar to that measured at₂₈₈ about $36\,\mathrm{kHz}$ on the same sample.

B. Mechanical loss at cryogenic temperatures

After the initial room temperature measurements, the 294 mechanical loss of the QM and FZ disks was measured at cryogenic temperatures. In turn they were individually placed inside a small pulse-cooled cryostat capable of 295 cooling down to 4 K. The cryostat housed a GeNS, simi-296 lar to the one used for room temperature measurements, with an identical silicon spherical lens held in a recess in the top of a stainless steel post. A temperature cycle of 297 the cryostat was carried out with calibrated temperature sensors mounted on the sample and on the post close 299 to the silicon lens. This allowed a temperature calibration curve to be created so that the sample temperature

could be determined from the temperature of the post. The temperature sensor on the sample was removed for mechanical loss measurements.

The mechanical losses of several resonant modes of both the QM and FZ disks were measured over a range of temperatures between 20 K and 290 K. The procedure of several repeat measurements providing an average loss with error bars given by the standard deviation was the same as for the room temperature measurements. The QM disk was measured three times over the full temperature range, with the sample being re-balanced on the nodal support each time, to check for repeatability. Due to the time constraints of a full mechanical loss run over the entire temperature range ($\approx 1 \, \text{month}$), the FZ disk was only able to be measured once before it was needed for another study.

Figure 5 shows the mechanical loss as a function of temperature for four resonant modes of both samples. The mechanical loss of the QM disk shows a very similar trend to the losses measured for the FZ disk. For some resonant modes, the mechanical loss is lower than that of the FZ disk. At $20\,\mathrm{K}$ the lowest mechanical loss measured on the QM disk was 2.6×10^{-8} at $17.8\,\mathrm{kHz}$ which is marginally higher than the lowest loss measured at $36.81\,\mathrm{kHz}$ on the FZ disk of $\sim2\times10^{-8}$. At $120\,\mathrm{K}$ the losses of all the modes measured were below $\sim2\times10^{-7}$. The lowest loss measured on the QM disk ($\sim1.8\times10^{-8}$) was more than a factor of two lower than the lowest loss of $\sim4.3\times10^{-8}$ measured on the FZ disk.

The mechanical loss of the first two modes at 14.75 and 17.85 kHz of the QM disk was lower than that of the two higher frequency resonance modes at 36.01 and 60.21 kHz, whereas the opposite was true for the FZ disk. This may be related to the different crystal orientation of the samples as the QM disk was $\langle 100 \rangle$ orientated and the FZ disk $\langle 111 \rangle$ orientated. These results are nevertheless still very promising for the quasi-monocrystalline material, making it potentially relevant for use in cryogenic gravitational wave detectors.

In the following section we also present measurements of the optical absorption of this quasi-monocrystalline material, which is also significant in determining a materials suitability for gravitational wave detector mirrors.

IV. OPTICAL ABSORPTION MEASUREMENTS

The optical absorption of the quasi-monocrystalline silicon sample (the small QM cuboid in Fig. $\boxed{2}$ ≈40 mm in length) was measured using photothermal common-path interferometry (PCI) $\boxed{26}$. The PCI technique exploits thermally induced optical length changes, created by a strong pump laser beam at the wavelength of interest due to optical absorption. The thermal effect, read out by a weak probe beam different in wavelength, is directly proportional to the absorption of the substrate. The setup can be calibrated by using a substrate of known absorp-

Montana Instruments Cryostation s100 https://www.montanainstruments.com

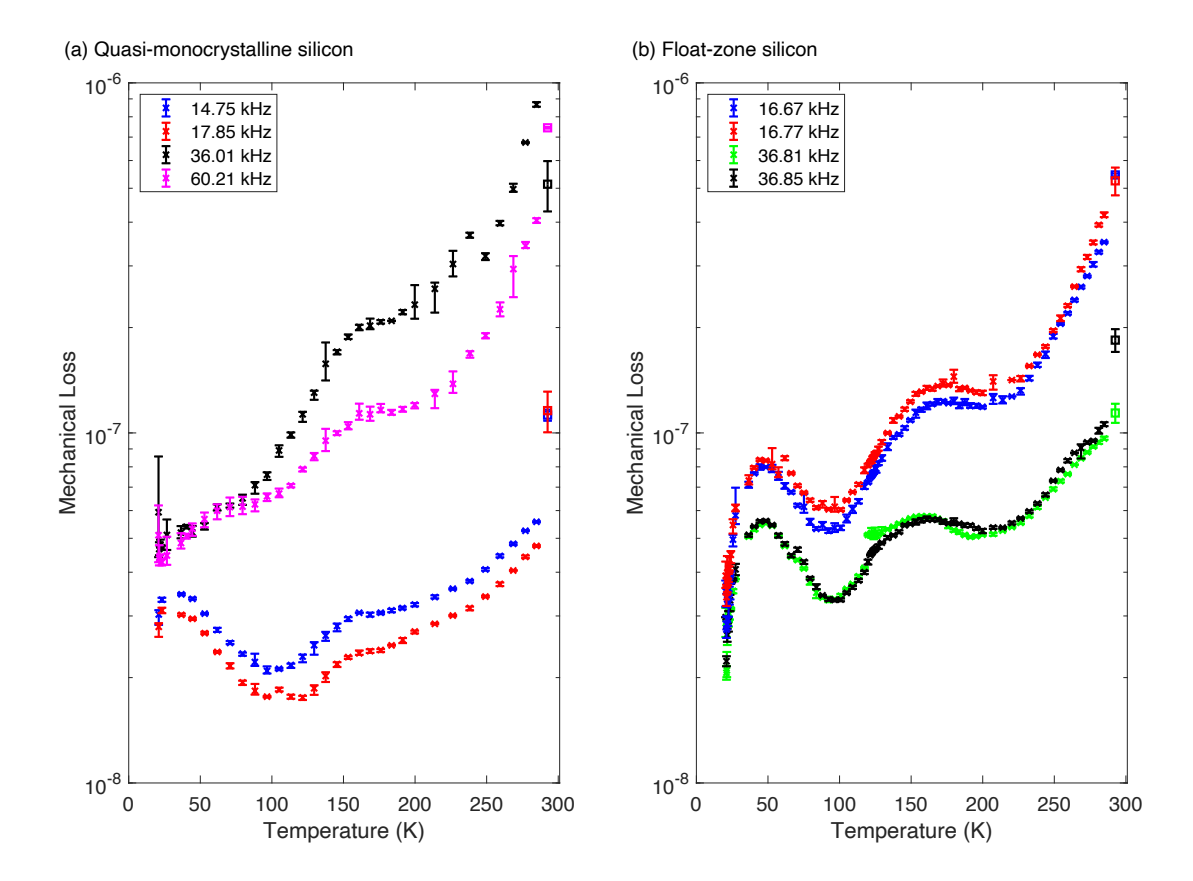


FIG. 5. Mechanical loss as a function of temperature, from $4\,\mathrm{K}$ to $300\,\mathrm{K}$, of the $50.8\,\mathrm{mm}$ diameter \times $5\,\mathrm{mm}$ thick QM disk (left) and FZ disk (right) samples.

tion, in our case made of fused silica.

An optical chopper is used to modulate the pump₃₂₉ beam, enabling phase information relative to this modu-₃₃₀ lation to be obtained, in addition to the amplitude of the₃₃₁ thermal effect. The phase is determined by the thermal₃₃₂ diffusion of the material and the geometric parameters of₃₃₃ the laser beams.

Based on the thermal diffusivity and the thermo-optic₃₃₅ parameters of the investigated substrate, e.g. our silicon₃₃₆ crystal, an additional factor is used to scale the ampli-₃₃₇ tude signal to the signal of fused silica. For silicon (and₃₃₈ the measurement/setup parameters used in this study),₃₃₉ this scaling factor is 0.42 for a phase of -8.5°. More de-₃₄₀ tail about the measurement procedure can be found in₃₄₁ literature [26] and on the company website [27].

Figure 6 shows the optical absorption measured at₃₄₃ 1550 nm (using a probe laser of wavelength 1620 nm) as₃₄₄ a function of position along the length of the small QM₃₄₅ cuboid. Measurements starting at three different posi-₃₄₆ tions on the surface were made, resulting in parallel scans₃₄₇ through the sample, represented by the three different₃₄₈

colours/line styles in Fig. 6(a). The vertical dashed lines mark the surface positions for the measurement represented by the green, dashed line. For the other scans, the position of the sample surfaces in the setup varied slightly.

For all three positions, the absorption shows a peak near the front surface (x-position of around $10-15\,\mathrm{mm}$) and decreases towards the back surface. To test if the peak near the front surface could be an artefact of the measurement technique, the sample was turned around and the measurement was repeated at two new positions (pink and purple lines in Fig. $\mathbf{G}(b)$). These measurements show the absorption peak at the back of the sample, indicating that one end of the sample does indeed have higher absorption than the other. Possible correlations with impurities are discussed in Sec. \mathbf{V} For comparison, the horizontal black line shows an absorption level of $\approx 9.6\%/\mathrm{cm}$ estimated from a simple transmission measurement.

Figures (c) and (d) show the phase signals corresponding to the absorption scans of the same colours in (a) and (b), where the red line indicates the phase expected for crystalline silicon.

From these measurements, we conclude an absorption of several 10%/cm at one end of the sample, and between $\approx 5 - 10\%$ /cm throughout the remainder of the

² Stanford Photo-Thermal Solutions www.stan-pts.com

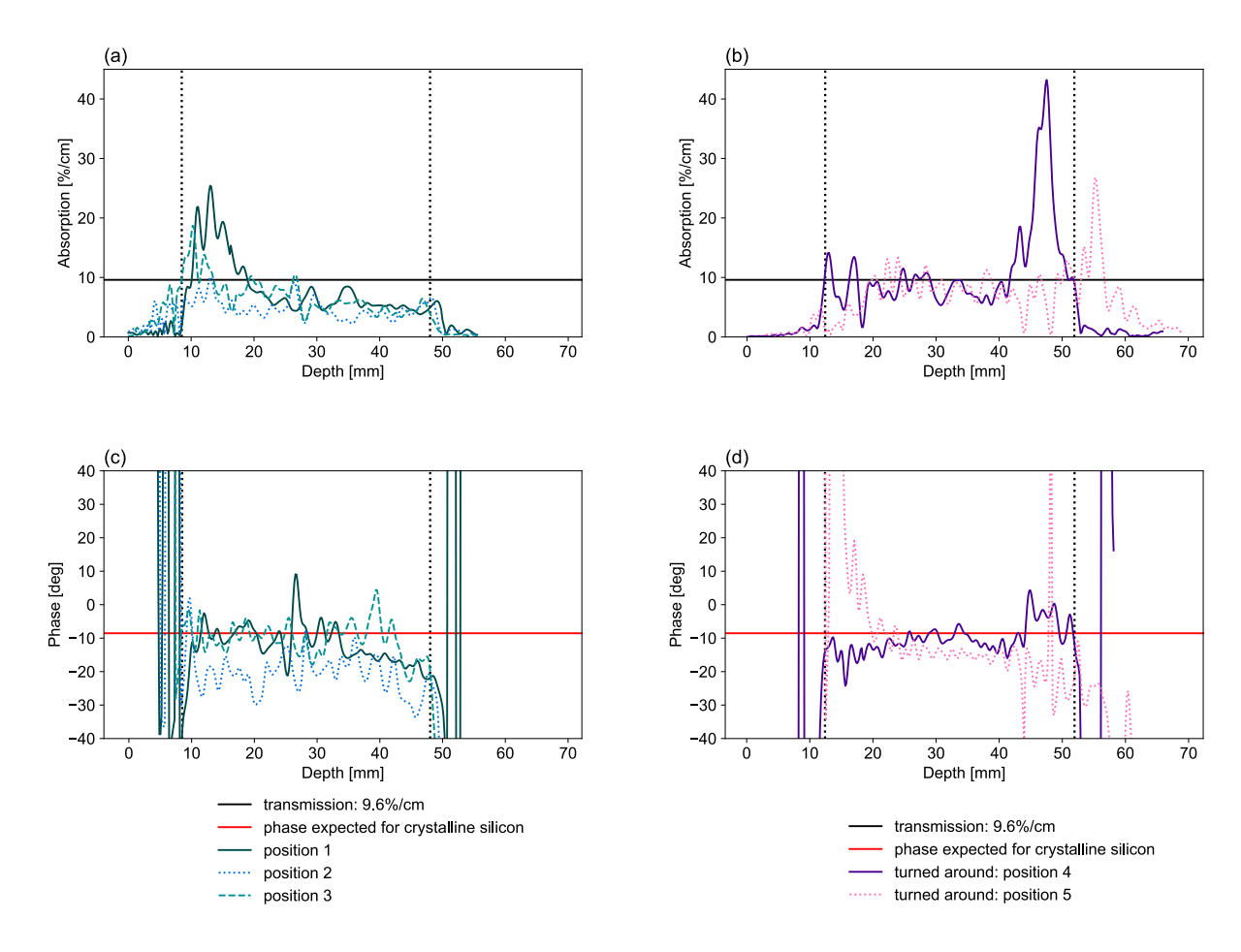


FIG. 6. (a) Optical absorption along the \approx 40 mm long small QM cuboid for entering the sample at three different positions indicated by the different colours/line styles. The dotted vertical lines indicate the surface positions for the measurements shown by the green, dashed line (the position of the sample front surface slightly varied between measurements). (b) Optical absorption scans through the sample at two different positions after turning the sample back surface to the front. (c) and (d) show the corresponding phase signals of those measurements. Outside the sample, the signal is meaningless: while the absorption signal becomes approximately zero, the phase shows large oscillations.

bulk of the sample, varying with position. An absorption 372 of $\approx 5\%$ /cm is consistent with a boron-doping level of $0.9\,\Omega\mathrm{cm}$ [13].

353

354

355

356

357

358

359

360

361

362

363

364

365

367

368

369

370

371

Non-linear absorption in silicon (arising from two pho-₃₇₄ ton absorption, and free carrier absorption due to carri-₃₇₅ ers produced by two photon absorption) can result in a₃₇₆ power-dependent absorption signal, potentially masking₃₇₇ the intrinsic absorption. To check for this, measurements₃₇₈ were repeated using a factor of two higher pump power.₃₇₉ No increase in the measured absorption was observed, in-₃₈₀ dicating that non-linear absorption does not make a sig-₃₈₁ nificant contribution to the measured absorption in this₃₈₂ measurement regime.

This absorption level is far too high for this material to₃₈₄ be used (for transmitted optics) in gravitational-wave de-₃₈₅ tectors. However, this material had not been optimized₃₈₆ for low optical absorption, which would be the next ob-₃₈₇ vious development step. In the following section, further₃₈₈ analysis of possible absorption sources is presented.

V. IMPURITY CHARACTERISATION

After the optical absorption measurements were carried out on the $\approx 40 \,\mathrm{mm}$ small OM cuboid, the minority carrier lifetime and the concentration of carbon and oxygen were determined to identify possible origins for the absorption. To carry out these examinations the small QM cuboid was cut lengthwise and polished on both sides using a chemo-mechanical polishing technique to a final thickness of $2510 \,\mu\mathrm{m}$. Existing markings on one end face (the marked side is set equal to the zero point) were retained to enable the measurements made in the longitudinal direction to be assigned true to location. Following the polishing, elevations were found close to the marked side. Using a light microscope the elevations were determined to be typical in shape and size for silicon carbide (SiC) inclusions, see Fig. 7. If this estimation is true, then a carbon concentration close to the solubility limit of carbon in silicon is also to be expected in the sur-

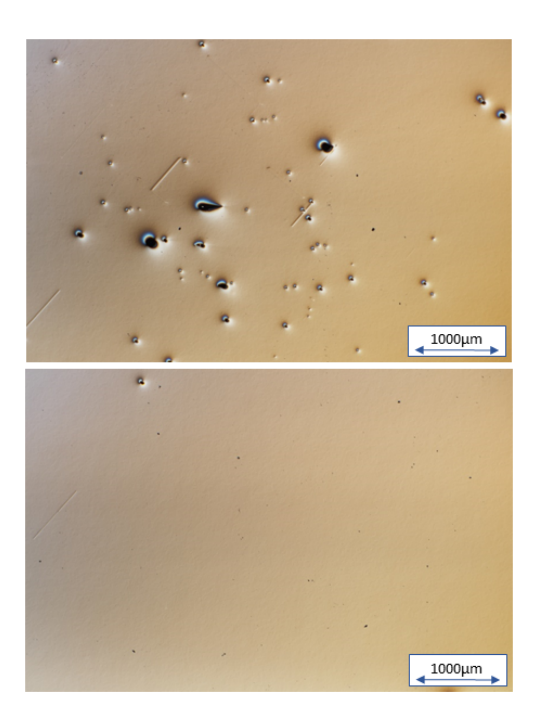


FIG. 7. Typical light microscopic image of SiC inclusions near the surface in the range of $0-10\,\mathrm{mm}$ of the sample (top), while almost no superficial features can be seen on the rest of the sample (bottom).

rounding material. The solubility limit in liquid silicon at melting temperature is $4.5 \times 10^{17} \, \mathrm{cm}^{-3}$ [27].

Exceeding the solubility limit in the melt leads to the formation of SiC particles, which can then be trapped at the growth interface as second phase particles and manifest themselves as inclusions. This formation and capturing process is well known [22, 23]. The trapping of the SiC particles in the middle of the growth process indicates insufficient mixing and can be avoided. This surface structuring is found only in the first quarter of the $\approx 40 \, \mathrm{mm}$ long sample, i.e. in the range from 0 to about $10 \, \mathrm{mm}$, while on the remaining surface of the sample almost no inclusions are detectable with the light field microscope (Fig. [7]).

Interstitial oxygen O_i and substitutional carbon $C_{S_{421}}^{--}$ in silicon are associated with typical absorption lines at $1107\,\mathrm{cm^{-1}}$ and $605\,\mathrm{cm^{-1}}$, respectively. The absorption spectra were measured axially along the sample by $_{424}^{--}$ Fourier-transform infrared spectroscopy (FTIR) using a $_{425}^{--}$ Bruker IFS 66 V under vacuum. Two measuring rows by different measuring point dimensions were carried out. Hoth measuring rows started from the marked side and continued beyond the sample. The first measuring row was carried out in a measuring distance of 1 mm with $_{429}^{--}$ an aperture of 2 mm which is the smallest possible with $_{430}^{--}$ the apparatus used, while the second measuring row was $_{431}^{--}$ carried out for reasons of smoothing with an aperture of $_{432}^{--}$ 3.5 mm in diameter with the same measuring distance of $_{433}^{--}$ 1 mm.

In Fig. 8, the carbon concentration is shown along the 435

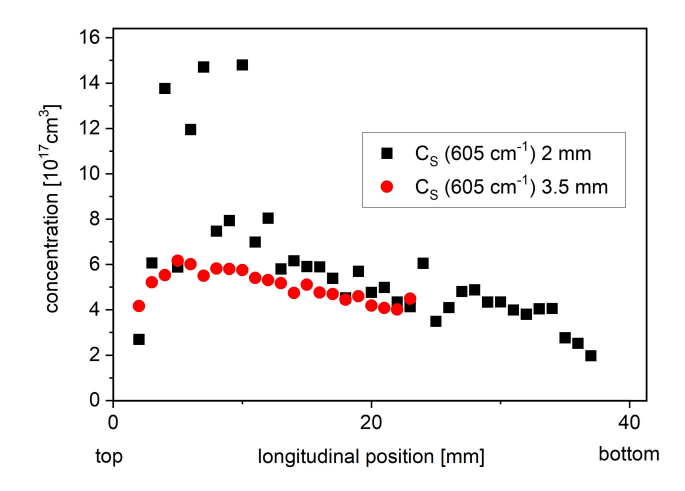


FIG. 8. FTIR measurement of $[C_S]$ in longitudinal direction with different apertures: blue 3.5 mm and red curve 2 mm.

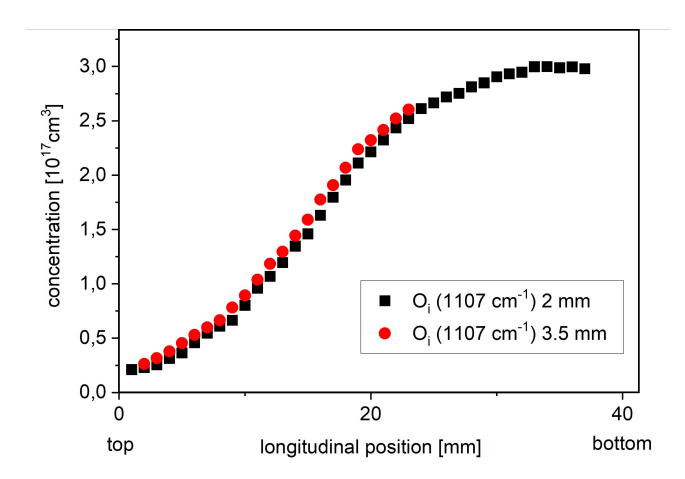


FIG. 9. FTIR measurement of $[O_i]$ in longitudinal direction with different apertures: blue $3.5\,\mathrm{mm}$ and red curve $2\,\mathrm{mm}.$

sample length starting from the marked side (zero) with optically observed inclusions. This marked side corresponds to the side with higher absorption in Fig. $\boxed{6}$. Both curves, measured with aperture 2 mm (red) and aperture 3.5 mm (blue), show the same shape and by use of the smaller aperture the measuring values do not make sense (measuring error amounts to approximately 5%). This might be due to scatter or/and absorption in the SiC inclusions.

Figure 9 shows analogously the oxygen concentration along the sample length measured with apertures of 2 mm (red) and 3.5 mm (blue), both showing an increase in the oxygen concentration from 2×10^{16} cm⁻³ to 3×10^{17} cm⁻³. During the directionally solidification growth, the oxygen concentration decreases in the direction of solidification in the ingot caused by the dominance of evaporation

over dissolution and a segregation coefficient larger than one [23]. Consequently, the sample orientation in the block in respect to the growth direction can be determined: the silicon at position 40 solidified first, named additionally with 'bottom' in Figs. 8 and 9. This also has consequences for the quality of the 2 inch disc used for mechanical loss measurements, where SiC inclusions should be present only in a rim area.

437

438

440

441

442

443

444

446

447

448

449

450

452

453

455

456

458

459

460

461

462

464

465

467

468

469

470

471

472

473

474

475

476

477

478

479

480

481

482

483

484

486

Measuring the interstitial oxygen and substitutional carbon concentration in smaller steps (1 mm) compared to the initial survey (see Sec. II) measurement with a distance of 1 cm, a locally unexpected lower interstitial oxygen concentration was detected in the area with significantly higher absorption, see Fig. 9 and 6. The absorption peak at this one end of the sample can neither be explained by the measured interstitial oxygen (too low) nor by the substitutional carbon (too homogeneous) concentrations. This local effect can probably be attributed to defect interaction, e.g. formation of oxygen precipitates during ingot cooling with presumably higher dislocation densities. To investigate the nature of this phenomena minority carrier lifetime was performed by the microwave-detected photoconductivity (MDP) method [28] on this polished non-passivated longitudinal sample. Figure 10 shows that the carrier lifetime is significantly reduced in the area of the SiC inclusions but shows otherwise typical lifetimes. The reduced lifetime might be due to a higher oxygen precipitation density [22], [29]. It can be assumed that the increased absorption at one end of the sample is due to defect interaction initiated by SiC inclusion. This formation of SiC can be avoided if the carbon input is significantly $^{*ot}_{488}$ reduced in an optimized growth process.

VI. DISCUSSION

491

Our results show that quasi-monocrystalline silicon can have very low mechanical loss, similar to the loss observed in high-purity float zone silicon. This suggests the material could meet the thermal noise requirements for cryogenic gravitational wave detectors, while also being available in the large diameters required (and beyond).

For example G7-type mono-like silicon ingots can be produced, the mass of which reaches 1200 kg with a square width of 1151 mm and a height of 390 mm [30]. However, the single-crystal area ratio and dislocation are the main problems associated with the mono-like technique. It has been shown in smaller ingots that dislocation gliding and propagation can be effectively controlled using \$\langle 110 \rangle\$-oriented seeds and the average \$\langle 100 \rangle\$ single crystal proportion has been increased over \$\langle 90 \%. An overview about seed-assisted growth of quasimonocrystalline silicon ingots and its challenges is given

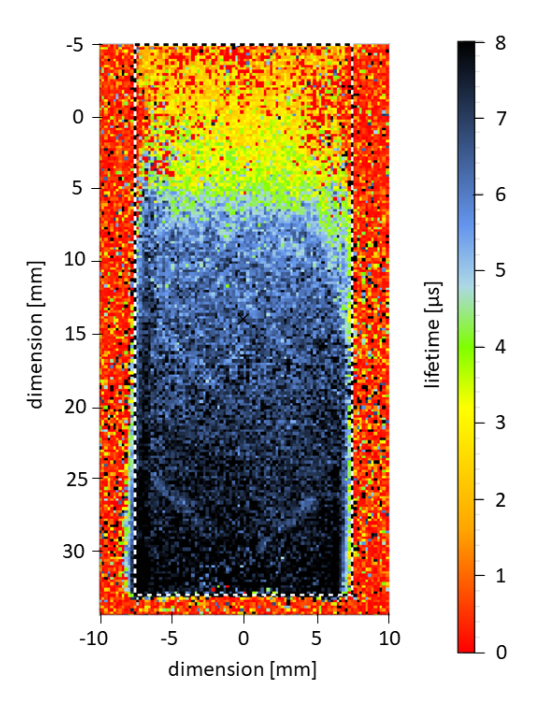


FIG. 10. Measurements of minority carrier lifetime on the now thinned $\approx 40\,\mathrm{mm}$ small QM cuboid (used previously for absorption measurements). The low values at the marked edge (here position -5 on the vertical axis) correspond to the high-absorption end.

in [31]. It should be noted that the mechanical loss was measured from a sample in a single-crystalline region of the quasi-monocrystalline ingot. Further development of the growth technique is likely to be required to ensure an area of mono-crystalline material large enough for a gravitational-wave detector test mass to be produced.

The optical absorption of our test material was found to be significantly higher than the value, of $\lessapprox~5$ – 10×10^{-6} /cm, usually thought to be required for a gravitational-wave detector mirror. However, it is interesting to note that only the 'input test masses' (ITMs) in the arm cavities of a gravitational-wave detector are required to transmit significant laser power. The 'end test masses' (ETMs) however, do not have significant power transmitted through them and somewhat higher absorption can therefore be tolerated in comparison to the ITMs. In a typical gravitational-wave detector configuration – with an ITM reflectivity of $\approx 99.5\%$ and an ETM reflectivity of $\approx 99.9995\%$ – the higher reflectivity of the ETM coating results in a factor of ≈ 200 less laser power being transmitted through the ETM than through the ITM. Therefore, we can tolerate a factor of 200 higher absorption in the ETM (resulting in $\approx 1 - 2 \times 10^{-3}$ /cm tolerable absorption).

The silicon investigated here was specifically boron-doped with a resistivity of $0.9\,\Omega{\rm cm}$ in order to achieve the desired resistance for solar cells and was not grown specifically with a view to a low level of (unintended)

³ The segregation coefficient is defined as the concentration ratio₅₁₃ of an impurity in a solid to this impurity in a liquid.

impurities potentially increasing the absorption at wave-549 lengths relevant for gravitational-wave detectors. The550 absorption throughout the majority of the length of the551 sample, of $\approx 5-10\,\%/\mathrm{cm}~(\approx 5-10\times 10^{-2}\,/\mathrm{cm}),$ was con-552 sistent with this doping level [13], except for one end of553 the sample with higher absorption which may be due to554 a higher concentration of carriers. An absorption reduc-555 tion of about two orders of magnitude would be required556 to make it a suitable ETM material.

515

516

517

518

519

520

521

522

523

525

526

527

528

529

531

532

534

535

537

538

539

540

541

543

544

546

547

548

580

581

582

583

584

587

588

589

590

591

592

593

594

595

596

597

598

If undoped and high-purity feedstock silicon is used,558 it is to be expected that the purity of the quasi-559 monocrystalline material can be significantly increased. 560 Nevertheless B, Al, and P, other metal impurities, such 561 as Fe, Co, Ni, and Cr, are quite common in quasi-562 monocrystalline silicon. They mainly come from the 563 crucible, its coating materials and the hot zone of $_{564}$ the furnace. To increase the resistivity and hence re-565 duce the bulk absorption by orders of magnitude, the566 impurity sources must be eliminated and the quasi-567 monocrystalline silicon ingot should be grown preferably with a very light p-doping. The standard crucible can be replaced by a high-purity fused silica crucible coated with a high-purity Si₃N₄ layers. The oxygen and carbon concentrations in the material get significantly lowered by an improved design of the hot zone with an optimised gas flow. Defect engineering includes an optimised growth 568 process and subsequent annealing of the ingot dissolving₅₆₉ precipitates and thermal donors that are present in the₅₇₀ as-grown material. Whether directionally solidified sil-571 icon can finally meet the absorption requirements of a_{572} mirror has to be investigated.

VII. SUMMARY

575

Quasi-monocrystalline silicon grown by directional so-578 lidification shows significant promise of being able to-579

meet the size and thermal noise requirements for cryogenic GWD mirrors. The optical absorption of the specific material studied here was high, as expected due to the doping, but it appears likely that with the use of pure feedstock, the absorption can be significantly reduced, at least to the point where this material would be suitable for use as an ETM mirror substrate in cryogenic gravitational wave detectors. Further research is required to determine if it may be possible to reduce the absorption sufficiently to allow this material to be used as an ITM mirror substrate. Another option may be increasing the size of the ETMs to beyond $\approx 50 \,\mathrm{cm}$ by using quasi-monocrystalline silicon which is available in larger diameters. Combining this with significantly smaller ITMs, similar to the configuration planned for Advanced Virgo upgrades [32], would then allow for different types of (pure) silicon potentially to be used as ITMs.

VIII. ACKNOWLEDGEMENTS

The authors thank N. Dropka, Ch. Frank-Rotsch, U. Juda, D. Linke, A. Lüdge, and R. Menzel for experimental support. This work was funded by the Bundesministerium für Wirtschaft und Energie (Federal Ministry of Economy and Energy, Germany) under the grant number 0325805c and by the Deutsche Forschungsgemeinschaft (DFG) under Germany's Excellence Strategy – EXC 2121 'Quantum Universe' – 390833306 and under DFG project STE 2646/1-1. We are grateful for financial support from STFC (ST/N005422/1, ST/V005634/1, ST/V001736/1) the Royal Society (RG110331) and the University of Glasgow.

B. P. Abbott, R. Abbott, T. D. Abbott, M. R. Aber-599 nathy, F. Acernese, K. Ackley, C. Adams, T. Adams, 600 P. Addesso, R. X. Adhikari, et al. (LIGO Scientific Col-601 laboration and Virgo Collaboration), "GW150914: The602 advanced LIGO detectors in the era of first discoveries," 603 Phys. Rev. Lett. 116, 131103 (2016).

F. Acernese et al., "Advanced Virgo: a second-generation interferometric gravitational wave detector," Classical and Quantum Gravity 32, 024001 (2015).

^[3] B. P. Abbott, R. Abbott, T. D. Abbott, S. Abraham,608 F. Acernese, K. Ackley, C. Adams, R. X. Adhikari, V. B.609 Adya, C. Affeldt, et al. (LIGO Scientific Collaboration610 and Virgo Collaboration), "GWTC-1: A gravitational-611 wave transient catalog of compact binary mergers ob-612 served by LIGO and Virgo during the first and second613 observing runs," Phys. Rev. X 9, 031040 (2019).

^[4] Yoichi Aso, Yuta Michimura, Kentaro Somiya, Masaki⁶¹⁵ Ando, Osamu Miyakawa, Takanori Sekiguchi, Daisuke⁶¹⁶ Tatsumi, and Hiroaki Yamamoto (The KAGRA Collabo-⁶¹⁷

ration), "Interferometer design of the kagra gravitational wave detector," Phys. Rev. D 88, 043007 (2013).

^[5] R. Abbott, T. D. Abbott, S. Abraham, F. Acernese, K. Ackley, A. Adams, C. Adams, R. X. Adhikari, V. B. Adya, C. Affeldt, et al. (LIGO Scientific Collaboration and Virgo Collaboration), "GWTC-2: Compact binary coalescences observed by LIGO and Virgo during the first half of the third observing run," Phys. Rev. X 11, 021053 (2021)

^[6] The LIGO Scientific Collaboration, the Virgo Collaboration, and the KAGRA Collaboration, "GWTC-3: Compact binary coalescences observed by LIGO and Virgo during the second part of the third observing run," (2021), arXiv:2111.03606 [gr-qc].

^[7] Gregory M Harry, Andri M Gretarsson, Peter R Saulson, Scott E Kittelberger, Steven D Penn, William J Startin, Sheila Rowan, Martin M Fejer, D R M Crooks, Gianpietro Cagnoli, Jim Hough, and Norio Nakagawa, "Thermal noise in interferometric gravitational wave de-

tectors due to dielectric optical coatings," Classical and 71 Quantum Gravity 19, 897–917 (2002).

618

619

620

621

622

623

624

625

626

627

628

629

630

631

632

633

634

635

636

637

638

639

640

641

642

643

644

645

646

647

648

649

650

651

652

653

654

655

656

657

658

659

660

661

662

663

664

665

666

667

668

669

670

- [8] M. E. Fine, H. van Duyne, and Nancy T. Kenney, "Low-673 temperature internal friction and elasticity effects in vit-674 reous silica," Journal of Applied Physics 25, 402–405 75 (1954).
- [9] E. Hirose, D. Bajuk, G. Billingsley, T. Kajita, B. Kestner, 677
 N. Mio, M. Ohashi, B. Reichman, H. Yamamoto, and 678
 L. Zhang, "Sapphire mirror for the KAGRA gravitational 679
 wave detector," Phys. Rev. D 89, 062003 (2014).
- [10] R. X. Adhikari, K. Arai, A. F. Brooks, C. Wipf,681
 O. Aguiar, P. Altin, B. Barr, L. Barsotti, R. Bassiri,682
 A. Bell, et al., "A cryogenic silicon interferometer for683 gravitational-wave detection," Classical and Quantum 684
 Gravity 37, 165003 (2020).
- [11] M. Abernathy, F. Acernese, P. Ajith, B. Allen, P. Amaro-686 Seoane, N. Andersson, S. Aoudia, P. Astone, B. Krish-687 nan, L. Barack, et al., "Einstein gravitational wave tele-588 scope (ET) conceptual design study," (2011).
- [12] M. A. Green and M. J. Keevers, "Optical properties of food intrinsic silicon at 300 k," Progress in Photovoltaics: Respectively search and Applications 3, 189–192 (1995).
- J. Degallaix, R. Flaminio, D. Forest, M. Granata, 693
 C. Michel, L. Pinard, T. Bertrand, and G. Cagnoli, 694
 "Bulk optical absorption of high resistivity silicon at 695
 1550 nm," Opt. Lett. 38, 2047-2049 (2013).
- [14] D.F. McGuigan, C.C. Lam, R.Q. Gram, A.W. Hoffman,697 et al., "Measurements of the mechanical q of single-698 crystal silicon at low temperatures," Journal of Low Tem-599 perature Physics 30, 621-629 (1978).
- [15] W. von Ammon, "FZ and CZ crystal growth: Cost driv-701 ing factors and new perspectives," physica status solidi⁷⁰²
 (a) **211**, 2461–2470 (2014).
- [16] Zheng Lu and Steven Kimbel, "Growth of 450 mm di-704 ameter semiconductor grade silicon crystals," Journal of 705 Crystal Growth 318, 193–195 (2011).
- [17] R. Doering and Y. Nishi, eds., Handbook of Semicon-707 ductor Manufacturing Technology (2nd ed.) (CRC Press,708 2008).
- [18] H.-J. Schulze, H. Öfner, F.-J. Niedernostheide, 710 F. Lükermann, and A. Schulz, "Fabrication of IG-711 BTs using 300 mm magnetic czochralski substrates," 712 IET Power Electronics 12, 3870–3873 (2019).
- [19] I. Martin, A. Bell, J. Steinlechner, P. Murray, J. Hough,⁷¹⁴
 R. Schnabel, R. Robie, S. Rowan, S. Tait, A. Markosyan,⁷¹⁵
 M. Fejer, E. Gustafson, C. Wipf, and R. Adhikari, "De-⁷¹⁶
 velopment of silicon mirrors and coatings," (2017).
- [20] D. Linke, N. Dropka, F.M. Kiessling, M. König,718 J. Krause, R.-P. Lange, and D. Sontag, "Character-719 ization of a 75 kg multicrystalline si ingot grown in⁷²⁰ a KRISTMAG[®]-type g2-sized directional solidification⁷²¹ furnace," Solar Energy Materials and Solar Cells 130,¹²² 652 – 660 (2014).

- [21] K. Kutsukake, T. Abe, N. Usami, K. Fujiwara, K. Morishita, and Kazuo Nakajima, "Formation mechanism of twin boundaries during crystal growth of silicon," Scripta Materialia 65, 556–559 (2011).
- [22] H. J. Möller, T. Kaden, S. Scholz, and S. Würzner, "Improving solar grade silicon by controlling extended defect generation and foreign atom defect interactions," Applied Physics A 96, 207–220 (2009).
- [23] F.-M. Kiessling, F. Büllesfeld, N. Dropka, Ch. Frank-Rotsch, M. Müller, and P. Rudolph, "Characterization of mc-si directionally solidified in travelling magnetic fields," Journal of Crystal Growth 360, 81–86 (2012), 5th International Workshop on Crystal Growth Technology.
- [24] E. Cesarini, M. Lorenzini, E. Campagna, F. Martelli, F. Piergiovanni, F. Vetrano, G. Losurdo, and G. Cagnoli, "A "gentle" nodal suspension for measurements of the acoustic attenuation in materials," Review of Scientific Instruments 80, 053904 (2009).
- [25] R Nawrodt, A Zimmer, T Koettig, C Schwarz, D Heinert, M Hudl, R Neubert, M Thürk, S Nietzsche, W Vodel, P Seidel, and A Tünnermann, "High mechanical qfactor measurements on silicon bulk samples," Journal of Physics: Conference Series 122, 012008 (2008).
- [26] A. Alexandrovski, Martin Fejer, A. Markosian, and Roger Route, "Photothermal common-path interferometry (PCI): new developments," in *Solid State Lasers* XVIII: Technology and Devices, Vol. 7193, edited by W. Andrew Clarkson, Norman Hodgson, and Ramesh K. Shori, International Society for Optics and Photonics (SPIE, 2009) pp. 79 – 91.
- [27] F. Durand and J. C. Duby, "Carbon solubility in solid and liquid silicon - a review with reference to eutectic equilibrium," Journal of Phase Equilibria 20, 61–63 (1999).
- [28] B. Berger, N. Schüler, S. Anger, B. Gründig-Wendrock, J. R. Niklas, and K. Dornich, "Contactless electrical defect characterization in semiconductors by microwave detected photo induced current transient spectroscopy (MD-PICTS) and microwave detected photoconductivity (MDP)," physica status solidi (a) 208, 769-776 (2011).
- [29] H. J. Möller, L. Long, M. Werner, and D. Yang, "Oxygen and carbon precipitation in multicrystalline Si," phys. stat. sol. (a) 171, 175–189 (1999).
- [30] C. W. Lan, C. F. Yang, A. Lan, M. Yang, A. Yu, H. P. Hsu, B. Hsu, and C. Hsu, "Engineering silicon crystals for photovoltaics," CrystEngComm 18, 1474–1485 (2016).
- [31] P. Wang, C. Cui, D. Yang, and X. Yu, "Seed-assisted growth of cast-mono silicon for photovoltaic application: Challenges and strategies," Solar RRL 4, 1900486 (2020).
- [32] Jonathon Baird and Matteo Barsuglia, "Fine-tuning the optical design of the advanced virgo+ gravitational-wave detector using binary-neutron star signals," Galaxies 8 (2020), 10.3390/galaxies8040086.